A&A 521, L25 (2010)
DOI: 10.1051/0004-6361/201015129

Astronomy & Astrophysics
Special feature

Herschel/HIFI: first science highlights

Letter to the Editor

Gas morphology and energetics at the surface of PDRs: New insights with *Herschel* observations of NGC 7023⋆

C. Joblin[1,2], P. Pilleri[1,2], J. Montillaud[1,2], A. Fuente[3], M. Gerin[4], O. Berné[5], V. Ossenkopf[6,7], J. Le Bourlot[8], D. Teyssier[9], J. R. Goicoechea[10], F. Le Petit[8], M. Röllig[6], M. Akyilmaz[6], A. O. Benz[11], F. Boulanger[12], S. Bruderer[11], C. Dedes[11], K. France[13], R. Güsten[14], A. Harris[15], T. Klein[14], C. Kramer[16], S. D. Lord[17], P. G. Martin[13], J. Martin-Pintado[10], B. Mookerjea[18], Y. Okada[6], T. G. Phillips[19], J.R. Rizzo[10], R. Simon[6], J. Stutzki[6], F. van der Tak[7,20], H. W. Yorke[21], E. Steinmetz[22], C. Jarchow[22], P. Hartogh[22], C. E. Honingh[6], O. Siebertz[6], E. Caux[1,2], and B. Colin[17]

(Affiliations are available on page 5 of the online edition)

Received 1 June 2010 / Accepted 19 July 2010

ABSTRACT

Context. We investigate the physics and chemistry of the gas and dust in dense photon-dominated regions (PDRs), along with their dependence on the illuminating UV field.
Aims. Using *Herschel*/HIFI observations, we study the gas energetics in NGC 7023 in relation to the morphology of this nebula. NGC 7023 is the prototype of a PDR illuminated by a B2V star and is one of the key targets of *Herschel*.
Methods. Our approach consists in determining the energetics of the region by combining the information carried by the mid-IR spectrum (extinction by classical grains, emission from very small dust particles) with that of the main gas coolant lines. In this letter, we discuss more specifically the intensity and line profile of the 158 μm (1901 GHz) [C II] line measured by HIFI and provide information on the emitting gas.
Results. We show that both the [C II] emission and the mid-IR emission from polycyclic aromatic hydrocarbons (PAHs) arise from the regions located in the transition zone between atomic and molecular gas. Using the Meudon PDR code and a simple transfer model, we find good agreement between the calculated and observed [C II] intensities.
Conclusions. HIFI observations of NGC 7023 provide the opportunity to constrain the energetics at the surface of PDRs. Future work will include analysis of the main coolant line [O I] and use of a new PDR model that includes PAH-related species.

Key words. ISM: structure – ISM: kinematics and dynamics – ISM: molecules – submillimeter: ISM

1. Introduction

One main goal of the guarantee time key programme "Warm and dense interstellar medium" (WADI) of the HIFI heterodyne spectrometer (de Graauw et al. 2010) onboard *Herschel* (Pilbratt et al. 2010) is to investigate the physics and chemistry of the gas and dust in dense photon-dominated regions (PDRs), as well as their dependence on the illuminating UV field. As part of this programme, we observed a prototype PDR, NGC 7023. The region is illuminated by the B2Ve HD 200775 [RA(2000) = 21h01m36.9s ; Dec(2000) = +68°09′47.8″], and has been shaped by the star formation process leading to the formation of a cavity. NGC 7023 has been widely studied at many wavelengths. It has been shown that this region hosts structures at different gas densities: $n_{\rm H} \sim 100\,{\rm cm}^{-3}$ in the cavity, $\sim 10^4\,{\rm cm}^{-3}$ in the PDRs that are located north-west (NW), south (S) and east, and 10^5–$10^6\,{\rm cm}^{-3}$ in dense filaments and clumps that are observed in the mm (Fuente et al. 1996; Gerin et al. 1998 and references therein) and near-IR (Lemaire et al. 1996; Martini et al. 1997).

NGC 7023 has been mapped by the instruments PACS and SPIRE of *Herschel* to study the emission of large cold grains (Abergel et al. 2010). We present here some observations of the gas at the surface of this nebula, taking advantage of the very high spectral resolution of HIFI. By combining these observations with previous mid-IR observations, we study the geometry and energetics of the NW and S PDRs.

2. Observations and results

2.1. HIFI observations

The HIFI observations presented here consist in (offset positions are relative to the star; see Fig. 1):

– single pointing using frequency switch mode towards the NW PDR in bands 1a and 3b. In band 1a, the frequency ranges covered by the wide band spectrometer (WBS) were [535–539] GHz (LSB) and [547–551] GHz (USB). In band 3b, covered ranges were [879–883] GHz (LSB) and [891–895] GHz (USB). The observed position ($\Delta\alpha$ = −25″, $\Delta\delta$ = +38″, called H_2 peak) corresponds to the peak intensity of the H_2 ro-vibrational emission associated to the near-IR filaments (Lemaire et al. 1996);
– on-the-fly (OTF) mapping of the [C II] 1901 GHz emission line in band 7b. The line was covered by both the WBS and the high-resolution spectrometer (HRS) in USB. Two cuts

⋆ *Herschel* is an ESA space observatory with science instruments provided by European-led Principal Investigator consortia and with important participation from NASA.

Table 1. Summary of the HIFI data.

Transition	$\nu_{\rm line}$ [GHz]	Position	Beam size [″]	$v_{\rm lsr}$ [km s^{-1}]	*FWHM*† [km s^{-1}]	$T_{\rm A}^{*}$ [K]	Area [K km s^{-1}]
HCO^+ (6–5)	535.062	H_2 peak	41	2.3 ± 0.3	1.4 ± 0.3	0.22	0.33 ± 0.07
^{13}CO (5–4)	550.926	H_2 peak	41	2.2 ± 0.3	1.2 ± 0.3	5.12	6.5 ± 1.5
^{13}CO (8–7)	881.272	H_2 peak	24	2.2 ± 0.2	0.9 ± 0.2	4.15	4.0 ± 0.8
$C^{18}O$ (5–4)	548.831	H_2 peak	41	2.1 ± 0.3	0.9 ± 0.3	1.12	1.1 ± 0.4
[C II]	1900.537	H_2 peak	11	2.7 ± 0.1	3.4 ± 0.2	23.6	85.6 ± 5.0
[C II]	1900.537	S-NW cut / North	11	2.5 ± 0.1	2.4 ± 0.2	17.9	45.8 ± 3.8
[C II]	1900.537	S-NW cut / Cavity	11	4.0 ± 0.1	2.2 ± 0.2	6.89	16.2 ± 1.4
[C II]	1900.537	S-NW cut / South	11	2.5 ± 0.1	2.4 ± 0.2	13.3	34.0 ± 2.8

Notes. $^{(\dagger)}$ For [C II] , we report the *FWHM* of the Gaussian profile of equivalent area and peak intensity.

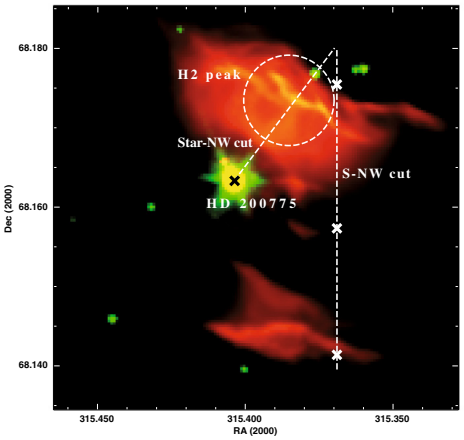

Fig. 1. The NW and S PDRs of NGC 7023 observed by *Spitzer*-IRAC at 8 μm (red) and 3.6 μm (green). The white circle represents the HIFI beam at 535 GHz (41″) towards the H_2 peak. The dotted lines show the cuts that are studied in the [C II] emission line at 158 μm with a beam of 11″, whereas white crosses indicate the specific positions reported in Fig. 2 and Table 1. The star position is shown with a black cross.

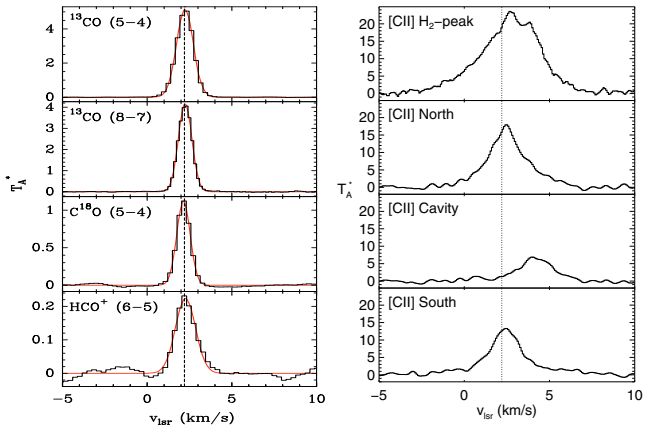

Fig. 2. *Left*: ^{13}CO, $C^{18}O$, and HCO^+ high-J transitions observed with HIFI toward the H_2 peak. *Right*: examples of [C II] emission profiles at the H_2 peak and at the three positions shown by crosses on Fig. 1: north ($\Delta\alpha = -47''$, $\Delta\delta = +45''$), cavity ($\Delta\alpha = -47''$, $\Delta\delta = -20''$), and south ($\Delta\alpha = -47''$, $\Delta\delta = -80''$), with offsets relative to the star position. In both figures, the vertical dotted line indicates $v_{\rm lsr} = 2.2$ km s^{-1}.

were performed: a cut from the star to the NW PDR (star-NW cut) and a south-north cut (hereafter S-NW cut) covering the NW PDR, the cavity and the S PDR ($\Delta\alpha = -47''$, $-85 < \Delta\delta < +60''$, see Fig. 1). The pixel size after regriding is 6.5″.

All these observations include an OFF reference position in the western lobe of the cavity ($\Delta\alpha = -144''$, $\Delta\delta = -47''$). Data was reduced with HIPE 3.0 (Ott 2010) on level-2 data produced with the standard pipeline. For the pointed observations in bands 1a and 3b, manual steps consisted in stitching sub-bands, baseline removal, and correction for main beam efficiency ($\eta_{\rm mb} = 0.71$). The [C II] WBS spectra required defringing, which was performed with standard HIPE tasks, and the best data quality was produced with the subtraction of two sinusoidal fringes. To verify the biases introduced by the fringe removal, we compared the WBS and HRS profiles, which showed good agreement both in profile and absolute intensity except for the weakest lines ($T_{\rm a}^{*} \lesssim 4$ K).

2.2. Gas kinematics

Figure 2 (left panel) shows the ^{13}CO 5–4, ^{13}CO 8–7, $C^{18}O$ 5–4, and HCO^+ 6–5 lines observed by HIFI towards the H_2 peak. All the lines have a central velocity of about 2.2 km s^{-1}, comparable to previous ground-based observations in several molecular lines (Fuente et al. 1993). Figure 2 (right panel) shows the [C II] line profiles at the H_2 peak and at different positions along the S-NW cut. The line is much broader than molecular lines and its profile shows a complex multi-component structure. The observations towards the PDRs show that the emission peaks at intermediate velocities ($v_{\rm lsr} \sim 1.8$–2.8 km s^{-1}), which have already been observed towards the NW PDR in several molecular tracers (see, for example, Fuente et al. 1996). There is also a contribution from higher velocity components ($v_{\rm lsr} \sim 4$ km s^{-1}), which dominate the emission in the cavity.

2.3. Emission from very small dust particles and C^+

The 158 μm (1901 GHz) [C II] and 63 μm [O I] lines are the major coolants of the gas at the surface of PDRs (Hollenbach & Tielens 1999). In these regions, photoelectric effect dominates the heating, while H_2 formation provides a minor contribution. Since the smallest dust particles, polycyclic aromatic hydrocarbons (PAHs) and very small grains (VSGs) contribute to a large fraction to this process (Bakes & Tielens 1994; Habart et al. 2001), and these particles emit in the mid-IR most of the energy they absorb in the UV, we expect that the mid-IR and [C II] emissions arise in the same regions.

We used mid-IR spectro-imagery data of the NW PDR of NGC 7023 that were obtained in the 5.5–14.5 μm range with the Infrared Spectrograph onboard *Spitzer* (Werner et al. 2004). For the S PDR, we used ISOCAM highly-processed data products (Boulanger et al. 1996) from the ISO data archive. To analyse the mid-IR spectra, we followed the method explained in Rapacioli et al. (2005) and Berné et al. (2007), in which the mid-IR emission is decomposed into three aromatic IR band

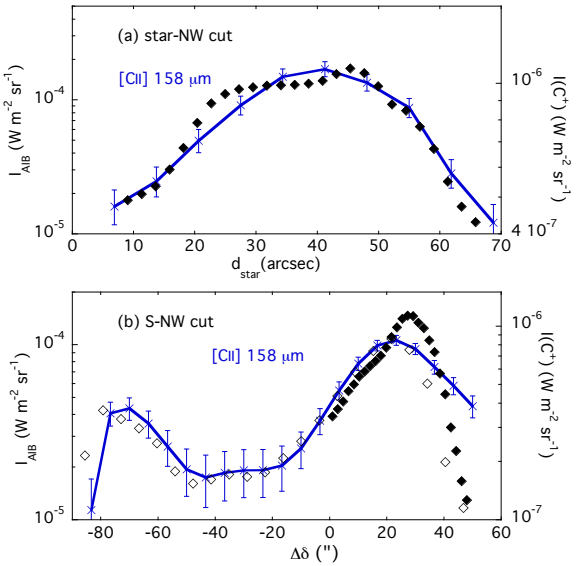

Fig. 3. Comparison between the [C II] 158 μm line flux (solid line) measured with HIFI at a beam size of 11″ and the aromatic IR band (AIB) flux (5.5-14 μm) along the star-NW **a)** and S-NW **b)** cuts. The error bars for [C II] are computed at one-sigma level. The AIB flux is determined with a fit of the mid-IR spectra using the three PAH-related populations shown in Fig. 5; filled diamonds are *Spitzer* data (1.8″ pix^{-1}), and open diamonds are ISOCAM data (6″ pix^{-1}).

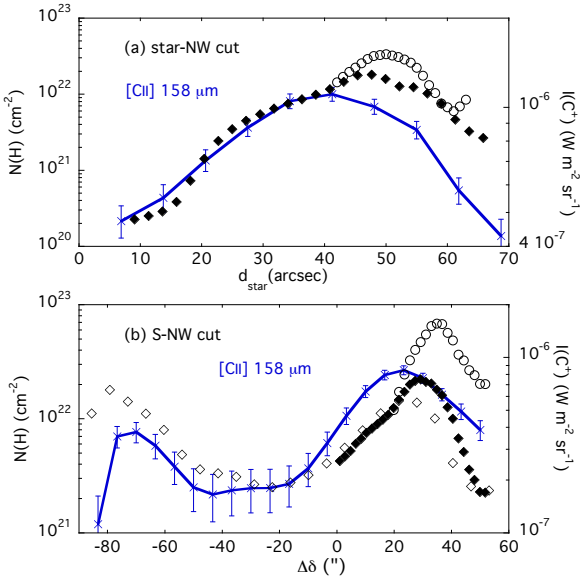

Fig. 4. Comparison between the [C II] 158 μm line flux (solid line) measured with HIFI at a beam size of 11″ and the column density N(H) along the star-NW **a)** and S-NW **b)** cuts. N(H) was derived from both the AIB flux (diamonds) and the mid-IR dust extinction (open circles); filled diamonds and open circles are *Spitzer* data (1.8″ pix^{-1}), and open diamonds are ISOCAM data (6″ pix^{-1}).

(AIB) spectra whose carriers are neutral PAHs (PAH^0), cationic PAHs (PAH$^+$), and evaporating VSGs. The fitting procedure was recently improved by including the convolution of the composite spectrum by extinction (Pilleri et al. 2010). Figure 3 displays the AIB flux, $I_{\rm AIB}$, obtained by summing the fluxes of the PAH^0, PAH$^+$, and VSG components that were derived from the fit. It shows that the AIB intensity correlates well with the [C II] line intensity, strongly suggesting that both emissions arise from the same regions. The fit of the mid-IR emission provides two independent tracers of the total gas column density N(H) along the line of sight as explained below.

(i) Owing to the excitation mechanism, the AIB intensity can be written as $I_{\rm AIB} \propto G_0 \times N^{\rm C}_{\rm AIB}$ where N^C_{AIB} is the column density of carbon in the AIB carriers and G_0 the UV flux in Habing units (Habing 1968). Assuming that $N^{\rm C}_{\rm AIB}/N$(H) stays constant at the PDR surface, $I_{\rm AIB}$ can therefore be used as a tracer of N(H) if G_0 is known (Pilleri et al. 2010).

(ii) If the column density N(H) is high enough, the effect of extinction by silicates can be seen on the AIB spectrum. In the mid-IR fit, the extinction is derived from a simple correction term, assuming that the emitting and absorbing materials are fully mixed: $\frac{1-e^{-\tau_\lambda}}{\tau_\lambda}$ where $\tau_\lambda = N({\rm H})\, C_{\rm ext}(\lambda)$ is the optical depth in the line of sight. The extinction cross-section per nucleon $C_{\rm ext}(\lambda)$ is taken from Weingartner & Draine (2001) for $R_V = 5.5$ and N(H) is a free parameter of the fit.

Method (ii) is precise for column densities higher than $N({\rm H}) \sim 10^{22}$ cm^{-2}. Method (i) can probe lower column densities but has two limitations. The AIB emission needs to be corrected for the variation in the UV field G_0 to retrieve the value of N(H). This was done assuming that G_0 scales as the inverse squared distance to the illuminating star HD200775 and a value of $G_0 = 2600$ at 42″ from this star (Pilleri et al. 2010). We used the projected distance as an estimate of the true distance. This introduces an error that can be especially strong at positions close to the star in the plane of the sky. Figure 3 shows that the AIB emission stays almost constant at $d < 16''$, therefore we used this value as the minimum effective distance of the NW PDR to the star. Method (i) also needs to be calibrated since the local emissivity of the AIB carriers is not known precisely. Our approach was therefore to derive a calibration factor using the values obtained by method (ii) around position 42″ on the star-NW cut. The same calibration factor was used for all positions along the two cuts. Figure 4 shows that the column densities that were derived on the two cuts correlate quite well with the [C II] line intensity.

3. Modelling C$^+$ emission

The critical density for the [C II] 158 μm line is $n_{\rm crit} = 2500\,{\rm cm}^{-3}$ for collisions with H and therefore the line emissivity depends mainly on temperature for n>n$_{crit}$. We selected a few positions on the HIFI S-NW [C II] cut, three points on the NW PDR and two on the South PDR (cf. Table 2). The values of G_0 were determined as explained in Sect. 2.3, and we assumed a constant average density with two different values: $n_{\rm H} = 2 \times 10^4$ cm^{-3} that is characteristic of the molecular cloud (Gerin et al. 1998) and $n_{\rm H} = 7 \times 10^3$ cm^{-3} that was derived by Rapacioli et al. (2006) in their study of PAH-related species.

We used the 1D Meudon PDR code (Le Petit et al. 2006) to compute the gas temperature T at the cloud surface for all the selected positions (cf. Table 2). The values of T are used to calculate the C$^+$ level populations. Line intensities are then derived by integrating along the line-of-sight (perpendicular to model results) and by assuming uniform excitation conditions. The thickness of the observed regions leads to an optical depth $\tau \sim 1$, which implies that transfer effects must be taken into account. If we assume constant excitation conditions and gas properties along the line of sight, then τ and the line intensity can be computed.

The agreement between calculated and observed flux values is very good when using $n_{\rm H} = 7\times10^3$ cm^{-3}. In the NW PDR, the ratio is 1.0 for NW3 (16) and NW2 (12), and 1.4 for NW1 (−3). For the S PDR, a value of 2.3 is derived for the two positions,

Table 2. Summary of the PDR modelling of the [C II] emission for 5 points along the HIFI S-NW cut ($\Delta\alpha = -47''$).

Pos. ($\Delta\delta$) ($''$)	$d_{\rm proj}$ ($''$)	UV field [a] (G_0)	T [b] (K)	PAH^+/PAH^0 [c]	Ionization parameter (γ) [b] (10^3 G_0 $K^{1/2}$ cm^3)	N(H) [d] (10^{21} cm^{-2})	[C II] local emissivity [b] (10^{-21} W m^{-3})	[C II] flux HIFI (10^{-7} W m^{-2} sr^{-1})	[C II] flux Model [b] (10^{-7} W m^{-2} sr^{-1})
NW3 (16)	50	1873	337 / 333	1.9	11.0 / 29.5	10.5	4.4 / 1.4	8.0	11.0 / 8.0
NW2 (12)	48	1975	342 / 333	2.7	11.7 / 31.1	8.1	4.4 / 1.4	6.9	9.5 / 7.1
NW1 (–3)	47	2100	348 / 333	9.6	12.6 / 33.0	3.9	4.4 / 1.4	3.3	5.6 / 4.6
S1 (–63)	79	747	248 / 320	1.7	3.8 / 11.8	8.7	4.2 / 1.4	3.1	8.3 / 7.2
S2 (–73)	87	607	230 / 312	0.96	3.0 / 9.5	14.0	4.1 / 1.4	3.7	9.6 / 8.4

Notes. [a] Calculated using a projected distance and $G_0 = 2600$ at $42''$ from the star; [b] From the PDR model using $n_{\rm H} = 2 \times 10^4 / 7 \times 10^3$ cm^{-3}, respectively; [c] Given as the ratio of the mid-IR intensities shown in Fig. 5; [d] Derived from the analysis of the mid-IR emission spectra.

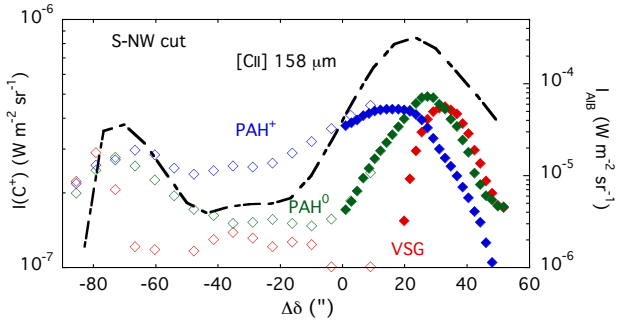

Fig. 5. S-NW cut in [C II] emission measured with HIFI at a beam size of $11''$(dot-dashed line) and distribution of the emission from the different very small dust populations, PAH^+ (blue), PAH^0 (green) and evaporating VSGs (red); filled diamonds are *Spitzer* data ($1.8''$ pix^{-1}) and open diamonds are ISOCAM data ($6''$ pix^{-1}).

suggesting that systematic effects are causing the deviation between observed and calculated values of the [C II] flux. There are several parameters that are not precise in our model but looking at Table 2, it seems the local [C II] emissivity is mainly affected by the local density and not by the value of G_0. For N(H), we assumed the same regions emit in PAHs and [C II] , in agreement with the profiles shown in Fig. 3. There is also an error for N(H) due to our method (cf. Sect. 2.3), but this error is expected to be the same for both PDRs. Dividing N(H) by a factor of two leads to lower values of the ratio of the calculated over the observed [CII] flux: 0.7−0.8 for the NW PDR and 1.6−1.7 for the S PDR.

One step further in the model would consist in studying the effect of the grain charge on the photoelectric efficiency (Bakes & Tielens 1994). The relative abundances of PAH^+, PAH^0, and evaporating VSGs vary significantly over the nebula (Fig. 5). Regions in the cavity appear mainly populated by PAH^+ (cf. NW1 (−3) in Table 2). Since the ionization potential of PAH^+ is much higher than that of PAH^0 (∼10 eV compared to ∼6 eV; Malloci et al. 2007), PAH^+ should contribute less to the photoelectric heating than PAH^0, leading to a decrease in the heating rate, hence in the gas cooling. In its current version, the PDR code uses classical grains with an MRN distribution (Mathis et al. 1977) and absorption and scattering cross-sections from Laor & Draine (1993). We have used grains of sizes from 15 Å to 3000 Å with a dust-to-gas mass ratio of 1%. As a result, the ionization parameter γ that quantifies the grain charge (cf. Table 2) does not reflect well the variations of the PAH charge observed in Fig. 5. An upgraded version, in which the PDR code is coupled to the code DUSTEM (Compiègne et al. 2010), is under development (Gonzalez et al., in prep.) and will allow for including PAHs. NGC 7023 is clearly a template region that could be used for these studies.

4. Conclusion

By using HIFI and complementary mid-IR data, we have shown that the [C II] cooling line and the AIB emission arise from the same regions, in the transition zone between atomic and molecular gas. The prototype PDR NGC 7023 was found to be a good object for comparison with PDR models. Further progress on the energetics of this region awaits for the coming [O I] data from the PACS instrument and a PDR model that treats the photophysics of PAHs consistently.

Acknowledgements. HIFI has been designed and built by a consortium of institutes and university departments from across Europe, Canada and the United States under the leadership of SRON Netherlands Institute for Space Research, Groningen, The Netherlands, and with major contributions from Germany, France, and the US. Consortium members are: Canada: CSA, U.Waterloo; France: CESR, LAB, LERMA, IRAM; Germany: KOSMA, MPIfR, MPS; Ireland, NUI Maynooth; Italy: ASI, IFSI-INAF, Osservatorio Astrofisico di Arcetri- INAF; Netherlands: SRON, TUD; Poland: CAMK, CBK; Spain: Observatorio Astronímico Nacional (IGN), Centro de Astrobiología (CSIC-INTA). Sweden: Chalmers University of Technology - MC2, RSS & GARD; Onsala Space Observatory; Swedish National Space Board, Stockholm University - Stockholm Observatory; Switzerland: ETH Zurich, FHNW; USA: Caltech, JPL, NHSC. This work was supported by the German *Deutsche Forschungsgemeinschaft, DFG* project number Os 177/1–1. A portion of this research was performed at the Jet Propulsion Laboratory, California Institute of Technology, under contract with the National Aeronautics and Space administration.

References

Abergel, A., Arab, H., Compiègne, M., et al. 2010, A&A, 518, L96
Bakes, E. L. O., & Tielens, A. G. G. M. 1994, ApJ, 427, 822
Berné, O., Joblin, C., Deville, Y., et al. 2007, A&A, 469, 575
Boulanger, F., Reach, W. T., Abergel, A., et al. 1996, A&A, 315, L325
Compiègne, M., Verstraete, L., Jones, A., et al. 2010, ApJ, submitted
de Graauw, Th., Helmich, F. P., Phillips, T. G., et al. 2010, A&A, 518, L6
Fuente, A., Martin-Pintado, J., Cernicharo, J., & Bachiller, R. 1993, A&A, 276, 473
Fuente, A., Martin-Pintado, J., Neri, R., Rogers, C., & Moriarty-Schieven, G. 1996, A&A, 310, 286
Gerin, M., Phillips, T. G., Keene, J., Betz, A. L., & Boreiko, R. T. 1998, ApJ, 500, 329
Habart, E., Verstraete, L., Boulanger, F., et al. 2001, A&A, 373, 702
Habing, H. J. 1968, Bull. Astron. Inst. Netherlands, 19, 421
Hollenbach, D. J., & Tielens, A. G. G. M. 1999, Rev. Mod. Phys., 71, 173
Laor, A., & Draine, B. T. 1993, ApJ, 402, 441
Le Petit, F., Nehmé, C., Le Bourlot, J., & Roueff, E. 2006, ApJS, 164, 506
Lemaire, J. L., Field, D., Gerin, M., et al. 1996, A&A, 308, 895
Malloci, G., Joblin, C., & Mulas, G. 2007, A&A, 462, 627
Martini, P., Sellgren, K., & Hora, J. L. 1997, ApJ, 484, 296
Mathis, J. S., Rumpl, W., & Nordsieck, K. H. 1977, ApJ, 217, 425
Ott, S. 2010, in Astronomical Data Analysis Software and Systems XIX, ed. Y Mizumoto, K. I. Morita, & M. Ohishi, ASP Conf. Ser., in press
Pilbratt, G. L., Riedinger, J. R., Passvogel, T., et al. 2010, A&A, 518, L1
Pilleri, P., Montillaud, J., Berné, O., & Joblin, C. 2010, A&A, submitted
Rapacioli, M., Joblin, C., & Boissel, P. 2005, A&A, 429, 193
Rapacioli, M., Calvo, F., Joblin, C., et al. 2006, A&A, 460, 519
Weingartner, J. C., & Draine, B. T. 2001, ApJ, 548, 296
Werner, M. W., Uchida, K. I., Sellgren, K., et al. 2004, ApJS, 154, 309

[1] Université de Toulouse, UPS, CESR, 9 avenue du colonel Roche, 31028 Toulouse Cedex 4, France
e-mail: christine.joblin@cesr.fr
[2] CNRS, UMR 5187, 31028 Toulouse, France
[3] Observatorio Astronómico Nacional (OAN), Apdo. 112, 28803 Alcalá de Henares (Madrid), Spain
[4] LERMA, Observatoire de Paris, 61 Av. de l'Observatoire, 75014 Paris, France
[5] Leiden Observatory, Universiteit Leiden, PO Box 9513, 2300 RA Leiden, The Netherlands
[6] I. Physikalisches Institut der Universität zu Köln, Zülpicher Straße 77, 50937 Köln, Germany
[7] SRON Netherlands Institute for Space Research, PO Box 800, 9700 AV Groningen, The Netherlands
[8] Observatoire de Paris, LUTH and Université Denis Diderot, Place J. Janssen, 92190 Meudon, France
[9] European Space Astronomy Centre, Urb. Villafranca del Castillo, PO Box 50727, 28080 Madrid, Spain
[10] Centro de Astrobiología, CSIC-INTA, 28850 Madrid, Spain
[11] Institute for Astronomy, ETH Zürich, 8093 Zürich, Switzerland
[12] Institut d'Astrophysique Spatiale, Université Paris-Sud, Bât. 121, 91405 Orsay Cedex, France
[13] Department of Astronomy and Astrophysics, University of Toronto, 60 St. George Street, Toronto, ON M5S 3H8, Canada
[14] Max-Planck-Institut für Radioastronomie, Auf dem Hügel 69, 53121, Bonn, Germany
[15] Astronomy Department, University of Maryland, College Park, MD 20742, USA
[16] Instituto de Radio Astronomía Milimétrica (IRAM), Avenida Divina Pastora 7, Local 20, 18012 Granada, Spain
[17] IPAC/Caltech, MS 100-22, Pasadena, CA 91125, USA
[18] Tata Institute of Fundamental Research (TIFR), Homi Bhabha Road, Mumbai 400005, India
[19] California Institute of Technology, 320-47, Pasadena, CA 91125-4700, USA
[20] Kapteyn Astronomical Institute, University of Groningen, PO box 800, 9700 AV Groningen, The Netherlands
[21] Jet Propulsion Laboratory, Caltech, Pasadena, CA 91109, USA
[22] MPI für Sonnensystemforschung, 37191 Katlenburg-Lindau, Germany